

Correlations between quasi-coherent fluctuations and the pedestal evolution during the inter-edge localized modes phase on DIII-Da)

A. Diallo, R. J. Groebner, T. L. Rhodes, D. J. Battaglia, D. R. Smith, T. H. Osborne, J. M. Canik, W. Guttenfelder, and P. B. Snyder

Citation: *Physics of Plasmas* **22**, 056111 (2015); doi: 10.1063/1.4921148

View online: <http://dx.doi.org/10.1063/1.4921148>

View Table of Contents: <http://scitation.aip.org/content/aip/journal/pop/22/5?ver=pdfcov>

Published by the *AIP Publishing*

Articles you may be interested in

Three-dimensional equilibria and island energy transport due to resonant magnetic perturbation edge localized mode suppression on DIII-D

Phys. Plasmas **22**, 112502 (2015); 10.1063/1.4935486

Simulations of drift resistive ballooning L-mode turbulence in the edge plasma of the DIII-D tokamak

Phys. Plasmas **20**, 055906 (2013); 10.1063/1.4804638

Observation of ion scale fluctuations in the pedestal region during the edge-localized-mode cycle on the National Spherical Torus Experiment

Phys. Plasmas **20**, 012505 (2013); 10.1063/1.4773402

Intrinsic rotation generation in ELM-free H-mode plasmas in the DIII-D tokamak—Experimental observations

Phys. Plasmas **18**, 072504 (2011); 10.1063/1.3605041

Measurement of edge currents in DIII-D and their implication for pedestal stability

Phys. Plasmas **12**, 056123 (2005); 10.1063/1.1879992



COMPLETELY REDESIGNED!

PHYSICS TODAY

Physics Today Buyer's Guide
Search with a purpose.

Correlations between quasi-coherent fluctuations and the pedestal evolution during the inter-edge localized modes phase on DIII-D^{a)}

A. Diallo,^{1,b)} R. J. Groebner,² T. L. Rhodes,³ D. J. Battaglia,¹ D. R. Smith,⁴ T. H. Osborne,² J. M. Canik,⁵ W. Guttenfelder,¹ and P. B. Snyder²

¹Princeton Plasma Physics Laboratory, P.O. Box 451, Princeton, New Jersey 08543-0451, USA

²General Atomics, P.O. Box 85608, San Diego, California 92186-5608, USA

³Physics and Astronomy Department, P.O. Box 957099, Los Angeles, California 90095-7099, USA

⁴Department of Engineering Physics, 1500 Engineering Dr., Madison, Wisconsin 53706, USA

⁵Oak Ridge National Laboratory, P.O. Box 2008, Oak Ridge, Tennessee 37831, USA

(Received 8 December 2014; accepted 30 March 2015; published online 15 May 2015)

Direct measurements of the pedestal recovery during an edge-localized mode cycle provide evidence that quasi-coherent fluctuations (QCFs) play a role in the inter-ELM pedestal dynamics. Using fast Thomson scattering measurements, the pedestal density and temperature evolutions are probed on sub-millisecond time scales to show a fast recovery of the density gradient compared to the temperature gradient. The temperature gradient appears to provide a drive for the onset of quasi-coherent fluctuations (as measured with the magnetic probe and the density diagnostics) localized in the pedestal. The amplitude evolution of these QCFs tracks the temperature gradient evolution including its saturation. Such correlation suggests that these QCFs play a key role in limiting the pedestal temperature gradient. The saturation of the QCFs coincides with the pressure gradient reaching the kinetic-ballooning mode (KBM) critical gradient as predicted by EPED1. Furthermore, linear microinstability analysis using GS2 indicates that the steep gradient is near the KBM threshold. Thus, the modeling and the observations together suggest that QCFs are consistent with dominant KBMs, although microtearing cannot be excluded as subdominant. © 2015 AIP Publishing LLC. [<http://dx.doi.org/10.1063/1.4921148>]

I. INTRODUCTION

With the discovery of the H-Mode,¹ significant research has been undertaken to understand the formation of the edge pressure pedestal. The pedestal is a narrow zone just inside the last closed flux surface that exhibits reduced energy and particle transport.² The pedestal pressure can be considered as a boundary condition for the core and theoretical modeling predicts that the pedestal height has a strong influence on core fusion power.³ Hence, an understanding of the pressure pedestal height and width formation is important for the predictive capability of future fusion devices.

The maximum achievable pedestal parameters have been commonly observed to be limited by edge instabilities known as edge localized modes (ELMs) (see Ref. 4 and references therein). While the high heat and particle fluxes of ELMs pose a threat for the plasma-facing components' lifetime on future devices such as ITER, the pedestal height leading up to an ELM is much desired for optimum core performance. In present day tokamaks, ELMs provide a means to flush impurities and to prevent them from accumulating in the core. An understanding of the dynamic of the pedestal parameters leading up to an ELM is far from complete. As a result, research efforts have been intensified with the objective to probe the pedestal recovery for a better formulation of the physical mechanism in the pedestal formation.

The EPED1 pedestal model^{5,6} has been developed to predict the pedestal height and width in high performance (Type I ELMing or QH Mode) H-Mode plasmas. The model hypothesizes that the pedestal is constrained by: (a) onset of non-local Peeling-Ballooning (P-B) modes at low to intermediate mode number and (b) onset of nearly local Kinetic Ballooning Modes (KBM) at high mode number. The EPED model calculates both constraints directly, based on a set of scalar inputs which are used to construct series of model equilibria for the stability calculations. EPED has been compared to observations in more than 500 cases on 5 tokamaks, typically finding agreement between predicted and observed pedestal pressure to a standard deviation of 20%–30%.^{5–13} EPED is a static model, designed to predict the pedestal in its fully developed state, and it is typically compared to observations in the later stages of the ELM cycle (or in quiescent H-Mode). However, EPED can also be used as an efficient platform for separately calculating P-B and KBM constraints, which can be compared to time dependent observations, for example, to assess the dynamical approach to each of these constraints (e.g., in Refs. 9 and 12). While the approach to P-B instability during the ELM cycle has been widely investigated, the approach to the KBM limit is less well studied. Multiple machines observe that edge pressure gradient establishes fairly rapidly in the recovery phase after an ELM.^{11,14,15} In addition, AUG determined that the density gradient recovers faster than the temperature gradient for various fueling rates.¹⁶ Once the gradient recovers, the pedestal pressure has been observed to expand at nearly constant gradient until the next ELM.^{14,17} Previous experiments on

^{a)}Paper B11 2, Bull. Am. Phys. Soc. 59, 23 (2014).

^{b)}Invited speaker.

DIII-D have also shown that the pedestal pressure gradient tracks approximately the predicted KBM critical gradient prior to the ELM crash.^{9,12} To study the hypothesis of KBM regulating transport, experiments have been executed with the objective to resolve the pedestal gradient recovery on a very fast time scale while simultaneously characterizing edge fluctuations associated with the pedestal dynamics.

Here, we focus on both the pedestal electron density and temperature recovery after an ELM crash for various plasma currents and the associated edge fluctuations. This work represents the first detailed profile response analysis after an ELM crash as a function of plasma current (0.7 MA–1.6 MA) with the associated fluctuations correlated with the pedestal parameter dynamics. The results clearly show that the pedestal density gradient recovers on a 3–5 ms time scale for various plasma currents. The pedestal temperature gradient recovery, on the other hand, takes between 5 and 15 ms for the range of plasma currents investigated. Using the edge density fluctuation diagnostics, we observed onset of the quasi-coherent fluctuations (QCFs) when the temperature gradient reaches a threshold. Subsequently, the QCF correlates and tracks the temperature gradient evolution including its saturation until the next ELM.

These QCFs are found to be localized in the pedestal region and have magnetic signatures. These observations are consistent with the edge dynamic picture suggesting that the edge temperature gradient provides the necessary free energy to drive these quasi-coherent fluctuations, which in turn limit the pedestal parameters. These quasi-coherent fluctuations are reminiscent of those observed in other H-mode regimes^{18–20} (e.g., edge-harmonics oscillations in quiescent H-modes (QH), quasi-coherent modes in enhanced D_x H-mode (EDA), and the weakly-coherent mode in I-mode). The quasi-coherent mode (QCM) in C-Mod was recently observed to be localized in the lower part of the steep

gradient region and to regulate both particle and density transport.²¹ During the inter-ELM phase, however, the quasi-coherent fluctuations appear to be localized in the pedestal region and most importantly to track the pedestal temperature gradient dynamics. Applications of EPED1 to the pedestal dynamics show that the pressure gradient reaches the KBM critical gradient at approximately the time that the QCF fluctuations turn on. Saturation of the EPED predicted pressure gradient occurs when the observed temperature gradient saturates. In addition, a linear local microinstability analysis using GS2 indicates that the steep gradient is near the KBM threshold.

This paper presents the detailed profile evolutions made possible using the DIII-D bunch Thomson scattering system which is described in Sec. II. Section III describes the measurements of the inter-ELM fluctuations and provides characterization of the quasi-coherent fluctuations. Section IV correlates QCFs with the pedestal parameters dynamics. Comparisons of the edge parameter dynamics using the EPED1 framework are provided in Sec. V followed by an initial microinstability analysis using GS2. Finally, a summary and discussions are provided.

II. PEDESTAL PARAMETERS DYNAMICS

The experiments were carried out on the DIII-D tokamak at fixed $B_T = 1.9$ T for three plasma currents (0.7 MA, 1 MA, and 1.6 MA). These type I ELM discharges were run in a lower single null configuration with the ion $B \times \nabla B$ drift direction toward the X-point. Time histories of low and high plasma current cases are displayed in Fig. 1. These experiments were targeted at capturing the pedestal recovery after an ELM crash using the recently upgraded Thomson scattering system.²² To accurately resolve the inter-ELM dynamics, the lasers were fired in a bunch mode, which enabled temporal resolution of up to 100 μ s. This increase in temporal resolution is achieved by using multiple lasers in the same path

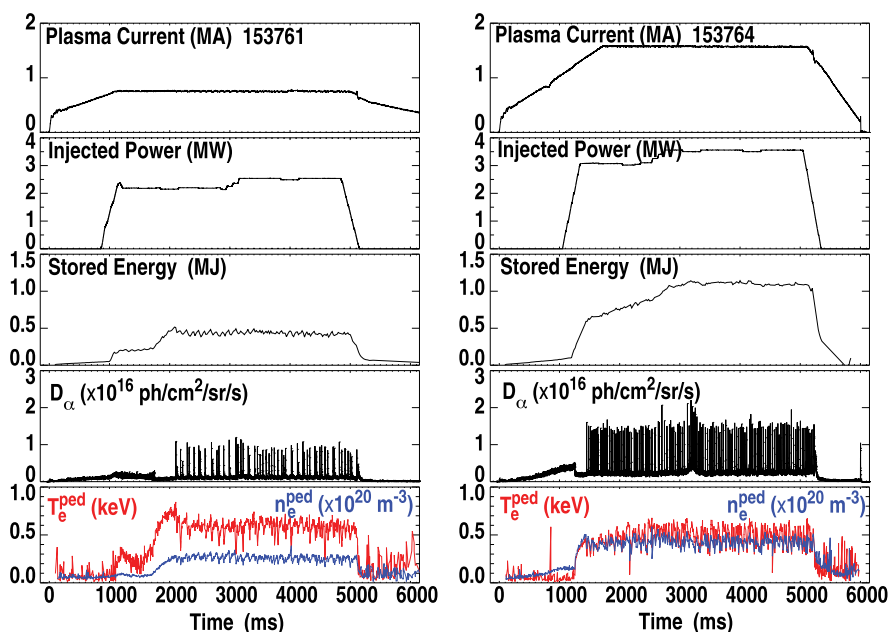


FIG. 1. Time history of the discharge parameters. Left panel represents the time history parameters of the low current ($I_p = 0.75$ MA) and the right panel those of the high current ($I_p = 1.6$ MA) case.

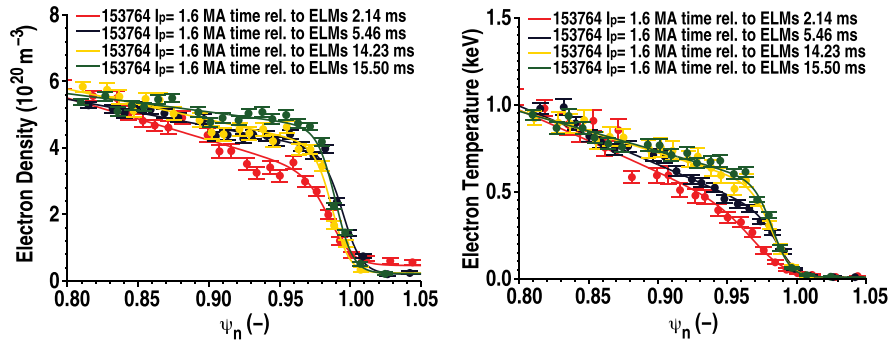


FIG. 2. Examples of density and temperature profile evolutions during the inter-ELM phase for the high current case ($I_p = 1.6$ MA).

with pulses interleaved closely in time. Normally, the lasers are phased to produce pulses at fairly regular intervals (exact regularity is not possible with the specific combination of 20 Hz and 50 Hz lasers being used). In bunch mode, the phase shifts are adjusted so that all lasers fire in rapid succession, followed by a cool down. This bunch mode encompasses between 3 and 7 laser pulses depending on the time in the discharges. To benefit from the high temporal resolution given by bunching the lasers, each profile is fitted using the modified-tanh. In addition, to minimize the errors resulting from mapping the data to the midplane, the fits are performed as a function of vertical physical position along the vertical laser chord. Given the enhanced spatial resolution recently implemented in the Thomson Scattering system,²² this approach enables the fits without relying on composite profiles. An example of the quality of the data is shown in Fig. 2, where the profile dynamics for the electron density and temperature are displayed.

Pedestal parameters, such as width and height, are obtained by fitting analytic functions to each time slice. These functions incorporate a tanh function to model the steep gradient region in the pedestal. The tanh function is smoothly joined to polynomial or spline functions to provide accurate fits to the profiles as they extend into the core

and into the scrape-off layer (SOL).²³ Figures 3 and 4 show the pedestal parameters (e.g., height and width) relative to the time after an ELM crash for the low and high current cases. For optimum statistics, we perform the analysis during the current flattop. For instance, for the low current case, the range is between 2048.6 ms and 5048.6 ms and for the high current case, the range is from 1380.2 ms through 5124 ms. It is evident from these figures that each ELM causes a prompt drop of the pedestal heights during which the widths expand. These width expansions vary from low to high current [Figs. 3(b) and 3(d) and Figs. 4(b) and 4(d)]. Finally, for completeness, the evolution of the radial electric field is obtained and displayed in Fig. 5. Note that such E_r evolution has been observed in Ref. 24. The dynamics of the radial electric field are key players for generating the transport barrier and consequently the pedestal observed in high confinement regimes. From Fig. 5, it is clearly seen that the radial electric field recovery time increases from ~ 6 ms to ~ 10 ms as I_p increases, which is consistent with the pressure gradient recovery (shown in Fig. 8). Below, we refer to *pedestal recovery time* as the time it takes for the pedestal parameters to reach their saturated values prior to the ELM onset.

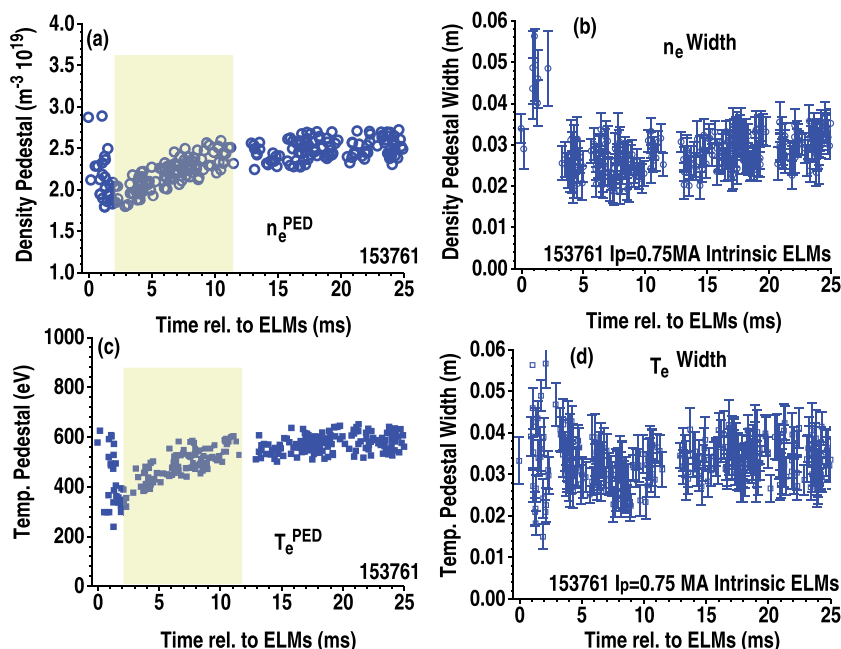


FIG. 3. Pedestal parameter evolution relative to an ELM crash for the low current case ($I_p = 0.75$ MA). (a) Density pedestal height; (b) density pedestal width; (c) temperature pedestal height; (d) temperature pedestal width. The shaded area represents the region where recovery of these parameters occurs.

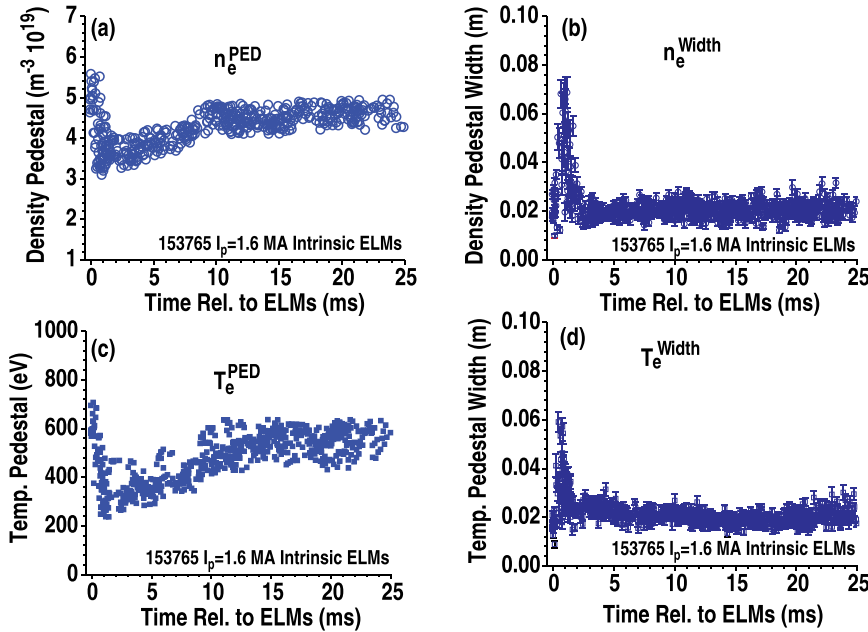


FIG. 4. Pedestal parameter evolution relative to an ELM crash for the high current case ($I_p = 1.6$ MA). (a) Density pedestal height; (b) density width; (c) temperature pedestal height; and (d) temperature pedestal width.

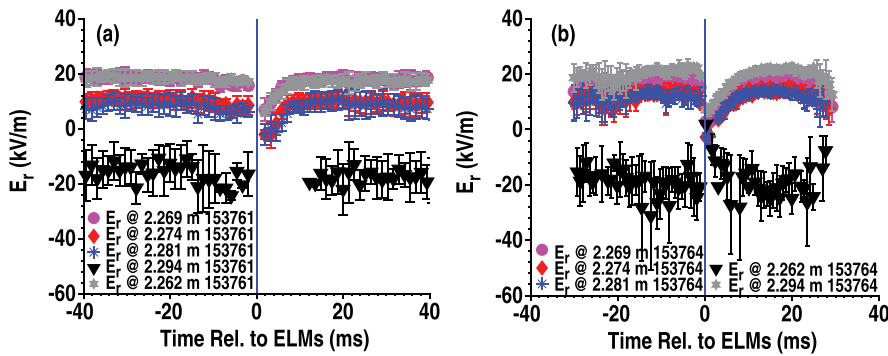


FIG. 5. The radial electric field dynamics during inter-ELM for (a) the low current case and (b) the high current case.

The variation of pedestal recovery time is clearly evidenced when the pedestal gradients are computed as shown in Figs. 6 and 7. In these figures, the evolution of both density and temperature gradients are displayed. In the low plasma current case (Fig. 6), the recovery time is highlighted for both the temperature and density gradients. Note that the density gradient recovers a little faster than that of the temperature. This difference in gradient recovery time is amplified when the plasma current is increased. For instance, at

high currents as shown in Fig. 7, the temperature gradient has a longer recovery time. It is worth noting that the ELM period decreases from low to high current. Based on the ELM period decrease, one would expect a longer than observed recovery time for the low current case. While this discrepancy in recovery time is not fully understood, we note that both the collisionality and the heating power have changed from low to high current which might affect the ELM period.

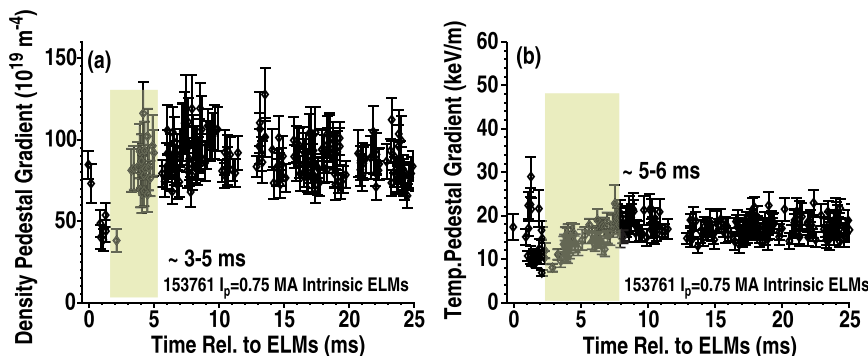


FIG. 6. Pedestal gradient evolution for the low current case. Here, the gradient is computed as the ratio of height to width. Inter-ELM dynamics of (a) the density gradient and (b) the temperature gradient.

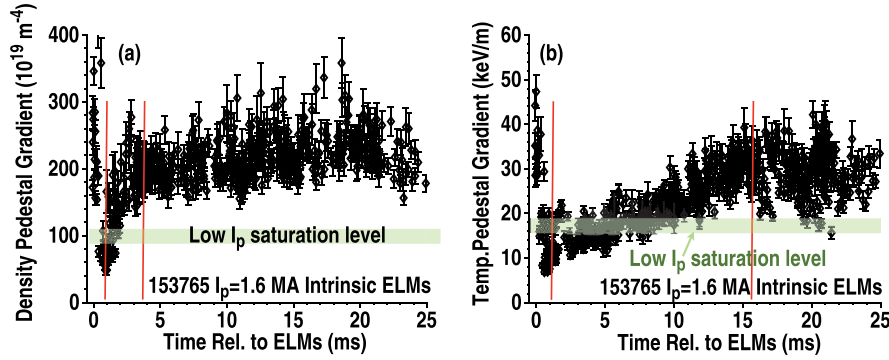


FIG. 7. Pedestal gradient evolution for the high current case. The horizontal shaded line represents the saturation level for the low current case. The vertical lines indicate the recovery of these gradients.

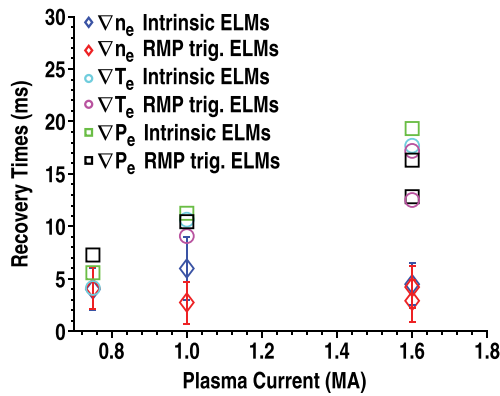


FIG. 8. Scaling of the pedestal recovery time with plasma current for both intrinsic and triggered ELMs. Note that triggered ELMs exhibit the same pedestal characteristics as intrinsic ELMs.

The recovery time is documented for three plasma current cases in Fig. 8. Note that the density recovery times appear to be independent of the plasma current. The temperature and the pressure gradients recovery times, on the other hand, increase with plasma current. In addition to the recovery time during intrinsic ELMs, we also probed the recovery time during non-resonant-magnetic-perturbation (RMP)-induced ELMs to improve the odds of capturing the inter-ELM dynamics using the Thomson scattering system in bunch mode. This was achieved by synchronizing the laser bursts with the imposed RMP currents. This RMP-induced ELM pacing approach was demonstrated in Ref. 25 in a wide range of plasma conditions. Here, ELM pacing was utilized to compare intrinsic and RMP-paced ELMs. In both cases the pedestal recovery time scale was similar. We then focused on intrinsic ELMs for the remainder of this paper.

With the detailed study of the edge parameters right after an ELM crash until the next ELM, the question arises: What transport mechanism limits the pedestal gradients?

III. INTER-ELM EDGE FLUCTUATIONS

Dedicated measurements of the edge fluctuations during the pedestal recovery have been performed to further investigate the limiting mechanism of the pedestal parameters. More specifically, the magnetic and density fluctuations are examined. Note that due to the high densities in these discharges, we were unable to obtain electron cyclotron emission (ECE) data at the edge.

Figure 9 shows the magnetic fluctuations using a Mirnov probe located 1 cm behind the boron nitride cover plate surface, which is located at $r = 98$ cm, $\theta = 50^\circ$ up from the midplane axis in a vacuum vessel coordinate system centered at $R = 167$ cm and $Z = 0$. The inter-ELM magnetic fluctuations preceding ELMs are shown in Figs. 9(a) and 9(b) for both plasma currents. In these plots, it can be clearly observed that after an ELM crash, there is a gap in the magnetic spectrograms followed by the onset of quasi-coherent fluctuations as indicated by the arrows. In Fig. 9(a), which represents the low current case, the quasi-coherent fluctuations appear on top of broadband fluctuations. In the high current case, on the other hand, two frequency bands are observed near 90 kHz and 120 kHz. Note that in Fig. 9(b), the low frequency (~ 50 kHz) has been determined to be due to a tearing mode or ELM unrelated events (more likely core fluctuations). Overall, there is clear evidence of quasi-coherent fluctuations preceding an ELM. Magnetic mode analysis for the low current case is shown in Fig. 10. Preceding the ELMs, the most dominant mode activities in Fig. 10 are $n = -2$ and $n = -3$. Here the negative direction

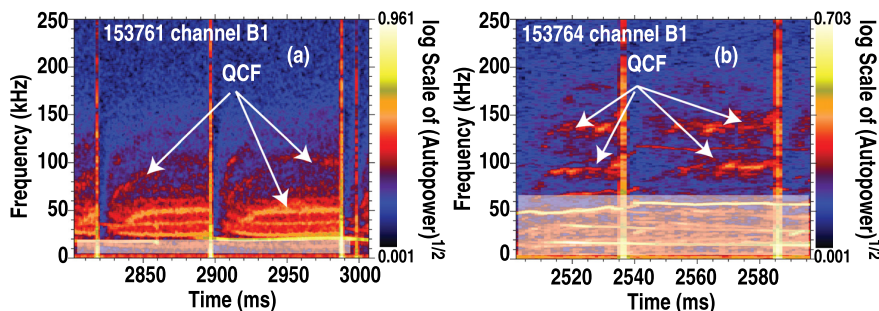


FIG. 9. Inter-ELM magnetic fluctuations spectrograms as measured using the Mirnov coils showing the QCFs in low (a) and high (b) current cases. The shaded areas on the spectrograms represent the core modes and broadband fluctuations which are not ELM related events.

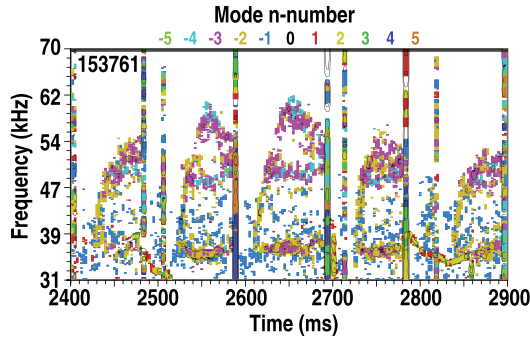


FIG. 10. For the low current case, the toroidal mode n -number analysis has been performed. Inter-ELM magnetic fluctuations n -numbers preceding the ELMs. Between ELMs, magnetic fluctuations with $n = -2, -3, -4$ occur in the frequency range of the QCF.

indicates propagation in the ion diamagnetic direction in the laboratory frame. Since the magnetic probes were sampled at 250 kHz, the high current case mode analysis could not be performed.

Similarly, on Alcator C-Mod, a QCF with electromagnetic signatures has been detected using a double-head probe located 2 cm from the separatrix.²⁶ On JET, similar quasi-coherent modes were observed as ELM-related events and were called washboard modes.^{27,28} There the modes showed multiple frequency spectra, hence their name “washboard modes.” On DIII-D, high frequency coherent (HFC) modes were observed in QH-mode plasmas with some features qualitatively similar to those expected for KBMs.²⁹ In addition, characteristics of a long poloidal wavelength and low frequency band of fluctuations were observed during ELM recovery. This saturation of these fluctuations is correlated with the electron pressure gradient,³⁰ qualitatively consistent with the expectations for KBMs. Finally, previous experiments on DIII-D indicated the onset of coherent modes on the beam emission spectroscopy (BES) diagnostics shortly after L-H transition,⁹ which appear to slow down the evolution of the pressure gradient leading up to the first ELM. Moreover, the pressure gradient is shown to be close to the KBM critical gradient when the modes are present.

The natural followup in characterization of this quasi-coherent mode is to provide its radial localization. For the low current case in Fig. 11(a), the BES inter-ELM fluctuation amplitude averaged between 20 and 120 kHz (encompassing the quasi-coherent mode) is displayed indicating radial localization of the fluctuation intensity in the pedestal region and more specifically near the pedestal top instead of the steep gradient. Definite localization, however, in either the pedestal top or the steep gradient region remains uncertain. In fact, these radial positions include the effects of the finite beam lifetime and viewing volume spot size. The EFIT mappings uncertainties are shown as horizontal bars in Fig. 11(b) with the points indicating the location of BES points. Note that the EFIT mapping uncertainty (of order 1–2 cm) mostly stems from the fact that the pedestal profiles are maps from data on the Thomson vertical chords to the mid plane radius to enable localization against other diagnostics.

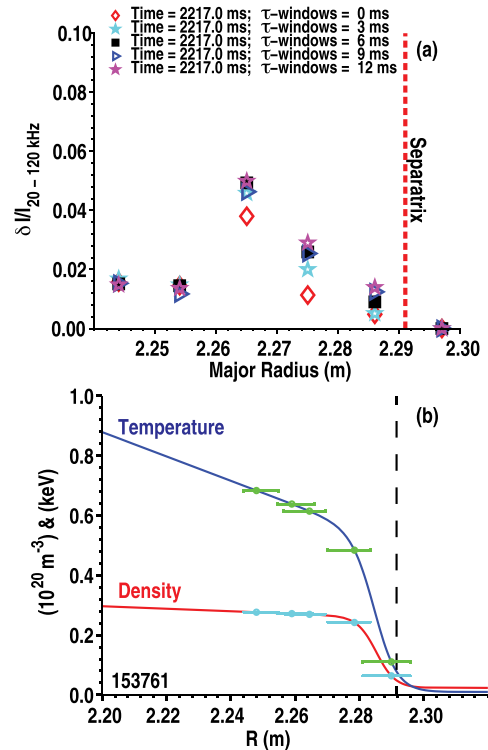


FIG. 11. BES signals $\delta I/I$ averaged over 20 kHz through 120 kHz for the low current case. (a) Radial profile of the amplitude evolution between ELMs. Here the symbols capture the time evolution. (b) Density and temperature profiles to indicate the BES measurements radial positions with measurement uncertainties as discussed in the text.

Similarly, in the high current case, as shown in Fig. 12, the QCF is localized in the pedestal region near the pedestal top as shown in Figs. 12(a)–12(c). For guidance, the bottom right panel of Fig. 12 shows the magnetic signatures. Note that here, the QCF appears to be localized in a rather narrow layer in the pedestal region. Overall, this QCF has strong magnetic signatures with weak associated density perturbation, which is localized in the pedestal region within uncertainties.

IV. CORRELATIONS BETWEEN INTER-ELM QUASI-COHERENT MODES AND THE PEDESTAL EVOLUTION

These observations of the QCF on the magnetic and density diagnostics provide the opportunity to test the correlation with the pedestal parameters’ evolution. To test any correlation between these QCF and the pedestal parameters, the amplitude of these fluctuations is extracted from the magnetic spectrogram and conditionally averaged with ELMs being the condition. These are then replotted as a function of time relative to an ELM. Figure 13(a) displays the magnetic spectrogram with the double arrow indicating the region of interest plotted on Fig. 13(b). This figure shows the conditionally-averaged amplitudes’ evolutions of the frequency band between 23 kHz and 60 kHz as a function of time relative to an ELM. Correlation of these amplitudes’ evolutions with the gradient of the pedestal temperature can readily be assessed. It is clearly seen that

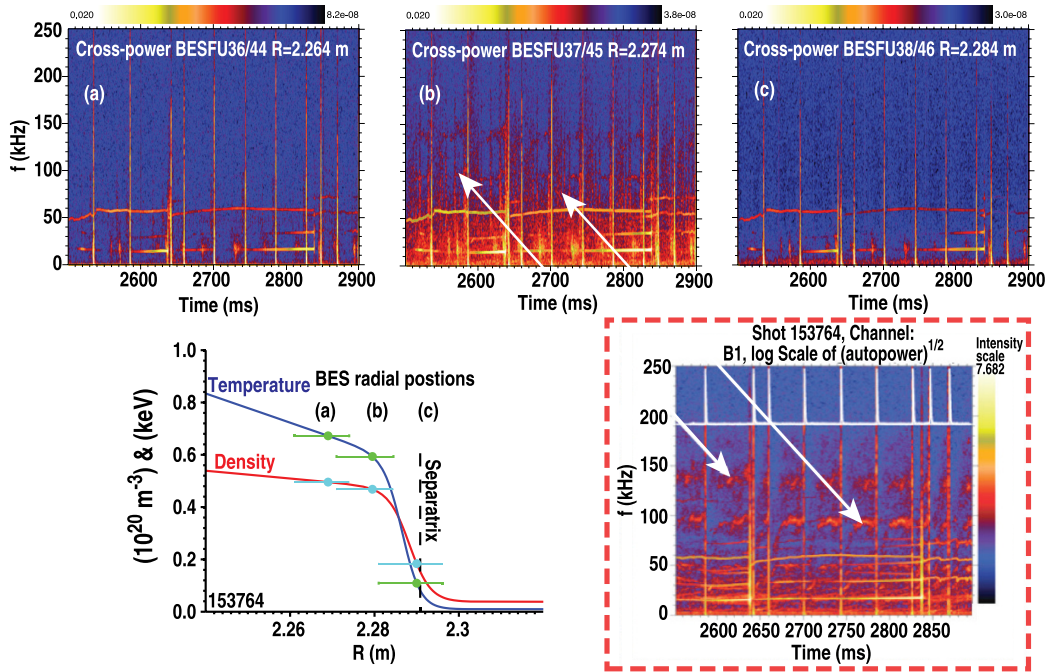


FIG. 12. Equivalent BES localization using cross-power analysis and comparison with the magnetic spectrograms indicating that the quasi-coherent fluctuations are localized at the pedestal top. ((a)–(c)) Crosspower spectrograms of poloidally separated BES channels for various radial channels. The corresponding radial points are indicated on the density and temperature profiles (bottom left panel). The bottom right panel shows the magnetic spectrograms during the same time for guidance.

the amplitude of the QCF onsets for a given temperature gradient and then monotonically increases until saturation is reached. Such saturation coincides with the temperature gradient saturation.

Figure 14(a) displays the temporal evolutions of the pedestal gradient and the scaled amplitude of the QCF between 120 and 170 kHz at the high current case. Note that this frequency band is the only one that correlated with gradient evolution. As can be seen in Fig. 14(a), there is clear onset of the QCF and a temporal evolution including its saturation which again coincides with the saturation of the gradient similar to the low current case. In Fig. 14(b), the amplitude of the QCF is plotted against the gradient to further emphasize the threshold gradient at which the QCF onsets. Overall, the QCF appears to be driven by temperature gradient in both the low current and high current case.

This correlation/coincidence with temperature gradient has also been observed on Alcator C-Mod,²⁶ pointing to a similar physical mechanism at play in both machines during the inter-ELM phase. It is worth noting that similar correlations of the BES broadband fluctuations with the gradients of pressure, density, and temperature have been observed previously on DIII-D in Fig. 10 of Ref. 30. A simple picture for halting the pedestal evolution is proposed. After an ELM crash, because there is very little local electron heating in the pedestal, electron heat mostly flows radially from the core through the pedestal. This heat contributes to building up the pedestal until a threshold gradient is reached. At that gradient, the onset of quasi-coherent fluctuations localized in the pedestal region provides the necessary transport to limit and saturate the pedestal gradient but allows the pedestal height and width to possibly increase until the peeling-ballooning

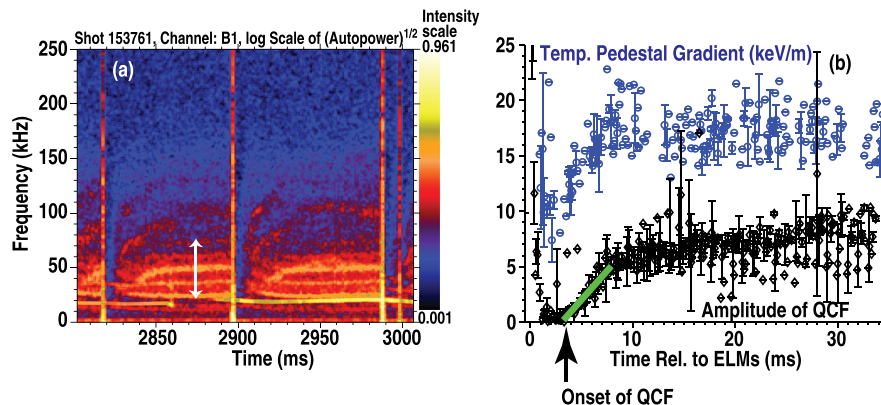


FIG. 13. Fluctuations amplitude correlations with pedestal gradients' evolutions for the low current case. (a) Magnetic fluctuation spectrogram with the vertical arrows indicating the QCF frequency bands to be considered for the amplitude analysis. (b) The QCF amplitude's evolution relative to ELM for the frequency bands 23–60 kHz. Overlaid in this plot is the temperature gradient evolution indicating the onset of the QCF amplitude evolution as represented using the back arrow.

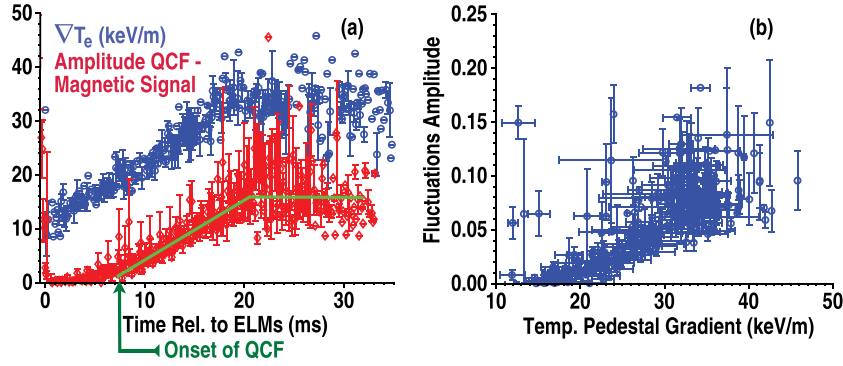


FIG. 14. Evolution of magnetic fluctuations and pedestal gradients during ELM recovery for high current case. (a) Scaled QCF amplitude evolution for the frequency band 120–170 kHz showing the onset. Overlaid is the temperature gradient evolution. (b) The QCF amplitude is plotted against the gradient evolution to show the threshold gradient.

boundary is reached and an ELM is triggered. Note that a time-dependent calculation between ELMs is needed to test this hypothesis and will be the subject of further work.

Doppler backscattering (DBS)^{31,32} is a diagnostic where a microwave beam is launched at a frequency that approaches a cutoff in the plasma and at an angle that is oblique to that cutoff. This diagnostic enables measurement of the density fluctuations at intermediate scale ($k_{\theta}\rho_s \sim 1$). For the low current case as shown in Fig. 15, the root-mean-square (rms) density fluctuations as measured using DBS show a drop of the rms level after an ELM crash followed by a quiet period lasting ~ 7 ms. Note that this time corresponds to the QCF amplitude evolution as shown in Fig. 13(b). After this period, the density fluctuations increase due to either pedestal density or temperature gradient recovery since for this low current case these gradient recovery times are similar. The probing scale corresponds to $k_{\theta}\rho_s \sim 0.9$ in the steep gradient region ($\psi_n = 0.95 \rightarrow 0.96$). For the high current case (not displayed here), the rms density fluctuations are observed to recover quickly within the same 5–7 ms. The DBS rms fluctuations at $k_{\theta}\rho_s \sim 0.03$ –0.1 are correlated with the density gradient in the steep gradient region.

Using BES poloidally separated views, one can also determine the poloidal correlation length of density fluctuations, which for the low current case yields an e-folding length of $\lambda_{\theta} \sim 5$ –6 cm, as shown in Fig. 16. In this figure, the poloidal correlation is computed starting from 5.1 ms after an ELM crash when the density gradient is recovered and when there is magnetic quasi-coherent fluctuations activity. The poloidal

scale is therefore indicative of the quasi-coherent fluctuation scale. This scale corresponds to $k_{\theta}\rho_s \sim 0.1$. The difference between DBS and BES in the estimates of $k_{\theta}\rho_s$ stems from the different radial regions probed by each diagnostic and the different wave numbers sensitivities. More specifically, the correlation length measured by BES was obtained for poloidally separated points shown in Fig. 11(a) corresponding to the pedestal top. The DBS channels, probing the pedestal recovery, measured fluctuations in the steep gradient $\psi_n = 0.95 \rightarrow 0.96$. In addition, BES correlation analysis yields the dominant turbulent wavenumber. DBS, on the hand, was tuned to only accept wavenumber $k_{\theta}\rho_s \sim 0.9$ in the steep gradient, which is higher than the dominant wavenumber observed by BES.

For completeness, BES data analysis in the high current case was performed to determine the poloidal wavenumber for the QCF frequency band (120–170 kHz) showing the best correlation with temperature gradient evolution (shown in Fig. 14). Figure 17 displays high coherency for the frequency band 120–170 kHz, which enables the determination of a poloidal/vertical wavenumber of $k_{\theta} \sim 0.18$ –0.2 rad/cm propagating in the electron diamagnetic direction in the laboratory frame. This propagation direction is still in the electron direction once the $E \times B$ velocity (~ 14 km/s) is taken into account. Note that if one accounts for potential misalignments due to mapping uncertainties (~ 2 cm) between

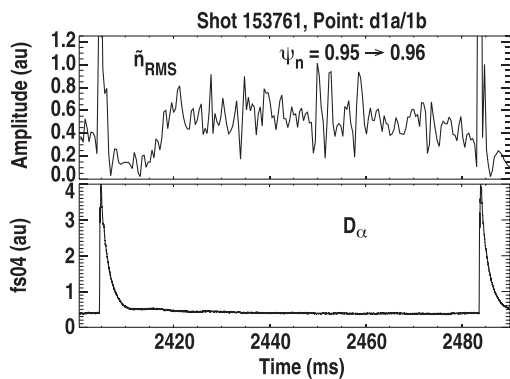


FIG. 15. Inter-ELM DBS rms fluctuations for the low current case. Note that these fluctuations are measured for $k_{\theta}\rho_s \sim 0.9$. In addition, these fluctuations are measured in the steep density gradient.

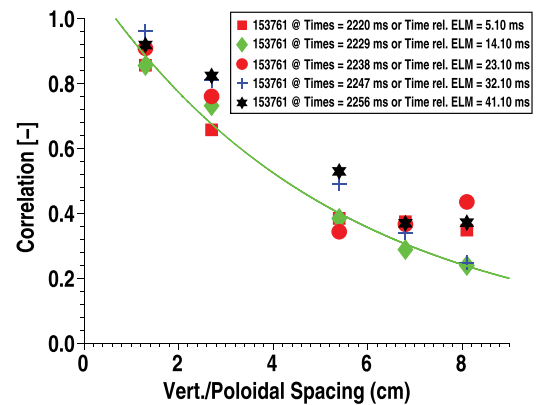


FIG. 16. Pair-wise BES channel correlations as a function of the vertical separations of the BES views between ELMs. A correlation length of 5–6 cm was determined, which correspond to $k_{\theta}\rho_s \sim 0.1$. The symbols capture the time evolution of the pair-wise cross-correlation coefficients as a function of vertical/poloidal separations.

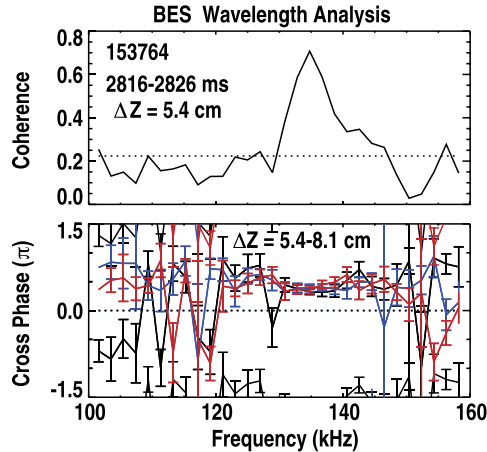


FIG. 17. Coherency and phase shift between poloidally separated BES views for the high current case. The top panel shows the coherency between two poloidally separated BES views ($\Delta z = 5.4$ cm). The bottom panel displays the phase shifts for three poloidal separations which yield poloidal wave-number of the QCF of $k_\theta = 0.18\text{--}0.2$ rad/cm with propagation in the electron diamagnetic direction.

BES, CER, Thomson scattering, this propagation direction could be in the ion diamagnetic direction.

In summary, for the high current case where the density and temperature gradient recovery times are more clearly distinct, we observe that the QCF onsets at a given temperature gradient threshold. The amplitude of the QCF tracks well the temperature gradient evolution including when the temperature gradient saturates. These fluctuations are pedestal localized and are of ion scale with $k_\theta \sim 0.18\text{--}0.2$ rad/cm with unresolved (due to potential mapping uncertainties) propagation direction in the plasma frame. Assessing the level of transport produced by these low- k fluctuations will require nonlinear gyrokinetic calculations in the edge which will be the subject of future work.

V. EPED1 PREDICTIONS AND MICROINSTABILITY ANALYSIS

This section utilizes the EPED1 framework to calculate P-B and KBM constraints, enabling comparisons to the observed pressure gradient evolution for both the low and high current case. Previous plasma current scans experiments on DIII-D provided tests of the EPED1 predictions and have shown reasonable agreement with measurements during the later part of the ELM cycle (Fig. 2 of Ref. 12). In addition, for plasma current of 0.5 MA, it was shown that the total pressure pedestal evolved along the KBM critical gradient (Fig. 5 of Ref. 12). Below, a similar approach is used to interpret the dynamic ELM cycle for both high and low current using EPED1. Note that EPED1 is a static model, designed to predict the structure of a fully developed pedestal. We use it here to provide a comparison of the observed gradient evolution to the calculated KBM constraint.

Figure 18 displays the gradient evolution against the time relative to an ELM. In each plot, the red squares indicate the binned averages of experimental data. From each of

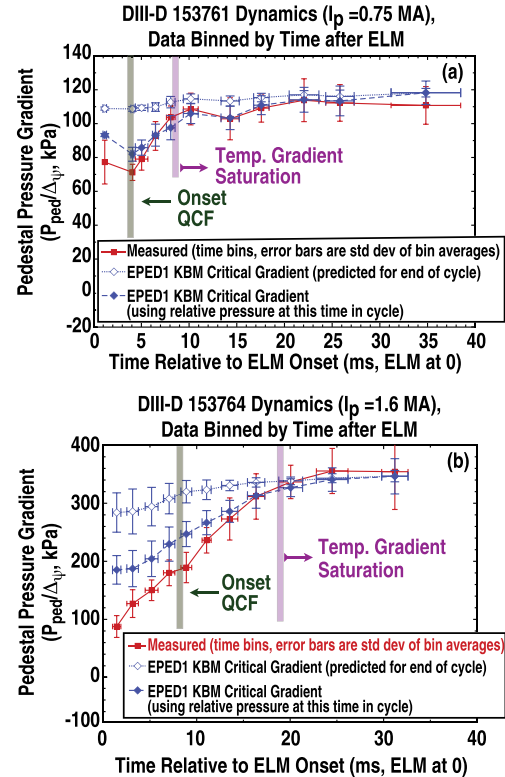


FIG. 18. EPED1 predictions for the low (a) and high current (b). The red squares represent the bin averages of DIII-D data for the pedestal pressure gradient evolution. The open blue symbols show the usual EPED1 predictions for the “final” pedestal height/width. The closed symbols give the EPED1 KBM constraint accounting for this time variation (see text for description). The vertical lines represent the time when the QCF onsets and when the temperature gradient saturates.

the data points, the EPED1 model requires eight input parameters, (B_T , I_p , R , a , κ , δ , global β , and n_e^{ped}) from which it outputs the pedestal pressure height and width (see Ref. 6 for further details). Here, given that experimental observations give fast measurements of n_e^{ped} and T_e^{ped} , the pressure pedestal is approximated by $2n_e^{ped}T_e^{ped}$ to track the dynamics. In Fig. 18, open blue symbols indicate the usual EPED1 predictions for the “final” (just prior to an ELM onset) pedestal height/width. These do change slightly with relative time because the EPED1 inputs (notably density) change a bit with relative time. This is a prediction of where the pedestal gradient should end up (and it agrees well with the later time data in both current cases). Again the error bars show standard deviations of bin averages (and the predictions vary because the inputs vary—these plots are the result of ~ 600 EPED1 calculations each with different inputs, put into time bins). While EPED1 is normally predicting the final state, we use it to investigate the time evolution. EPED1’s predicted KBM constraint scales like $(p_{ped})^{1/2}$ at a given poloidal field. Because $(p_{ped})^{1/2}$ is varying during the ELM cycle here, we can account for this variation by multiplying the EPED1 gradient by $\sqrt{(p_{ped}^{now}/p_{ped}^{final})}$, where p_{ped}^{now} is the pedestal pressure in the current time bin, and p_{ped}^{final} is the pedestal

pressure near the end of the ELM cycle. The closed blue symbols give the EPED1 KBM constraint accounting for this time variation. This represents a reasonable approximation of the KBM critical gradient at each given time bin.

Overall, EPED1 is predicting the final state well in both current cases, including a factor ~ 3 increase in gradient going from low to high current case. Figure 18(a) shows that the KBM critical gradient is quickly reached in the low current case consistent with the onset of QCF indicated using a vertical line. This onset time has been determined in Fig. 13(b). In addition, the saturation of the temperature gradient coincides approximately with EPED1 predictions of pressure gradient reaching the KBM critical gradient. Similarly, in the high current case, the onset of QCF and saturation of the temperature gradient are indicated using vertical lines in Fig. 18(b). In both cases, the onset of the QCF corresponds approximately (within expected uncertainties in the observations and the calculation) with the approach to the calculated KBM constraint. However, we note that the QCF appears slightly earlier than the best estimate of the EPED1 KBM constraint. We note that EPED1 is calculating a condition for KBM criticality, on average, across the pedestal, and hence we might expect that the KBM constraint would be reached locally somewhat before this time, though this is difficult to quantify precisely given the uncertainties. Overall, the observations in Fig. 18 are consistent with a physics picture in which the QCF onsets when KBM criticality is first approached locally, and then the temperature gradient fully saturates when the pressure gradient reaches KBM criticality across the pedestal, such that further increases in gradient within the barrier are constrained by the KBM (though the barrier may continue to broaden inward until the ELM occurs).

Initial linear microstability properties of these edge plasmas have been analyzed for the high current case using the initial value gyrokinetic code GS2.³³ To get an idea what kind of microinstabilities are likely to be responsible for driving the turbulence for our nominal parameters in various β regimes, we perform linear gyrokinetics calculation in the pedestal region. Note that extensive pedestal gyrokinetic calculations have been performed for NSTX³⁴

and MAST³⁵ using GS2 where the basic scaling analysis is laid out for an identification of the microinstabilities in the edge. We refer the reader to Ref. 34 for details about the GS2 analysis. Given that experiment localizes the QCF in the pedestal region, which encompassed the steep gradient region and the pedestal top, GS2 calculations are performed at the pedestal top and in the top 1/2 of the steep gradient region.

Figure 19(a) indicates the pedestal top where the GS2 calculations are performed. The growth rates and frequencies are displayed in Figs. 19(b) and 19(c). Electron β scans have been performed around the nominal operating point at $\beta_e = 0.34\%$. During the scan a mode pops out when β_e reaches 0.8%, which is far from the nominal experimental β_e . The sensitivity in β_e is used to determine KBM instability, which in this case suggests that the nominal point is KBM stable.

Similarly, in Fig. 20, GS2 calculations including a scan in β_e are displayed in the top 1/2 of the steep gradient region. In this radius ($r/a = 0.985$) at the top 1/2 of the steep gradient, the nominal experimental point is near the KBM threshold. Note that GS2 only determines the most unstable mode, which is found to be KBM here. Thus, the code cannot provide information about the possible existence of subdominant modes such as micro-tearing modes, which are predicted to also reside in the pedestal region as shown in Ref. 35. KBM instability in the steep gradient region has been reported in NSTX^{34,36} and MAST.³⁵ The real frequency indicates a propagation in the electron diamagnetic direction, which has been determined using extensive parameter scans to be a hybrid TEM/KBM in Ref. 34. This propagation direction agrees with BES estimates of the QCF propagation. Note that these local GS2 calculations are initial and that nonlocal effects are expected to play a role in the pedestal region. Using GEM, a global linear δf gyrokinetic code, and GYRO (another gyrokinetic code), similar simulations have been performed on the DIII-D H-mode discharges.^{37,38} Both of these simulations find evidence that the edge pedestal is KBM unstable. Future work should employ nonlinear global calculations for a true comparison with the observed saturated QCF.

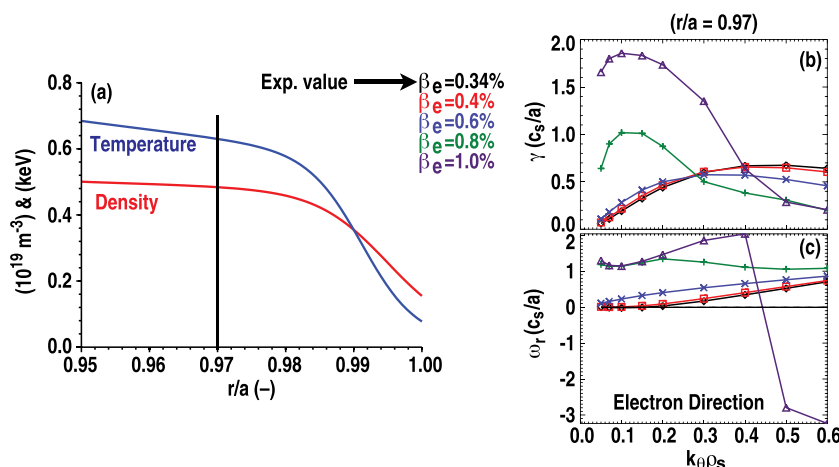


FIG. 19. (a) Radial profiles of the electron temperature and density (153764 - late in the ELM cycle) indicating the GS2 analysis region at the pedestal top. (b) Growth rate for multiple β_e from the nominal experiment value. (c) The associated real frequency.

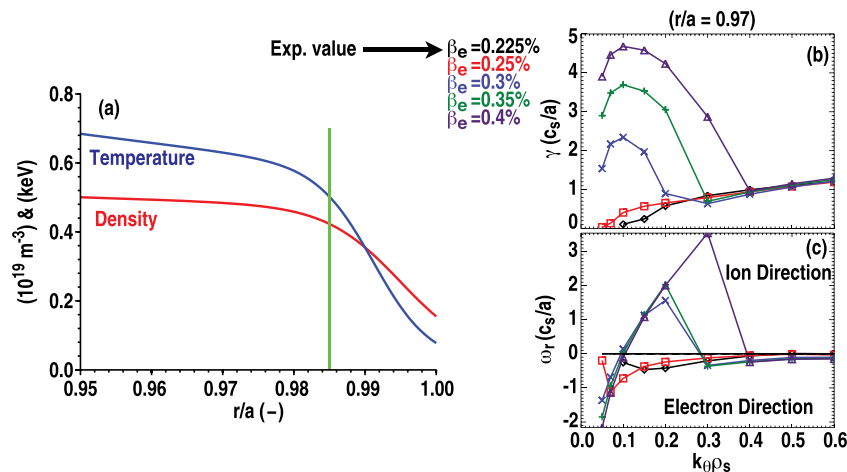


FIG. 20. (a) Radial profiles of the electron temperature and density (153764 - late in the ELM cycle) indicating the GS2 analysis region at top 1/2 of the steep gradient region. (b) Growth rate for multiple β_e from the nominal experiment value. (c) The associated real frequency.

VI. SUMMARY AND DISCUSSION

Detailed studies of the pedestal recovery after a type I ELM and associated edge fluctuations called quasi-coherent fluctuations are presented. The DIII-D Thomson scattering system was operated in bunch mode in order to obtain high time resolution measurements of pedestal recovery times after ELM events. The measurements were performed for a range of plasma currents (0.7, 1.0, and 1.6 MA) to show that the density gradient recovers on a shorter time scale than the temperature gradient at high current. In addition, the density gradient recovery time is shown to be independent of plasma current. One interpretation of these results is that edge recycling is responsible for the pedestal density gradient recovery. In fact, recent work by Ref. 39 using UEDGE-MB-W proposed that an intense particle deposition into the wall by the ELM followed by continuous gas release between ELMs at constant rate could provide a mechanism to fuel the pedestal in line with our observations. On the other hand, the temperature gradient recovery time increases with the plasma current. Note that both collisionality and heating power have also changed with current. These changes may have contributed to the longer recovery time. Modeling efforts to reproduce the recovery times will be the subject of future work.

The pedestal temperature gradient recovery is found to correlate with the onset of QCF observed in density and magnetic fluctuations between ELMs. The amplitude of the QCF is observed to onset when a threshold temperature gradient is reached both in low and high current, although it is more clearly seen for the high current case since the recovery times of the density and temperature gradients are distinct. Once the QCF onsets, its amplitude tracks well the temperature gradient evolution including saturation of both amplitude and gradient prior to the next ELM. While causality in the saturated state between amplitude and gradient is difficult to show at this point, the evolution of the fluctuations correlates well with the gradient pointing to QCF playing a key role in regulating the edge transport to “halt” the temperature gradient’s evolution (and linked to this evolution is the pedestal pressure gradient). Such edge regulation is speculated to occur through continuous release of energy across the plasma boundary. The quasi-coherent fluctuations are determined to be $n = -2$ and $n = -3$

toroidal modes in the low plasma current case. Unfortunately, no mode number analysis could be determined in the high current case due to the lack of magnetic diagnostic spectral resolution (low sampling rate of the Mirnov coils).

Furthermore, the quasi-coherent fluctuations are measured to be localized at the pedestal top of temperature using the BES but could also be localized in the pedestal within measurement uncertainties. Correlation measurements indicate that the dominant edge fluctuations, including the quasi-coherent fluctuations, are low $k_{\theta}\rho_s = 0.03 - 0.1$ for the low and high plasma current cases. Similar density fluctuations measurements using the DBS system detected rms density fluctuations with intermediate $k_{\theta}\rho_s = 0.9$. Note DBS was mostly probing the steep gradient region. The QCFs are low- k , localized in the pedestal region with unresolved propagation direction, onset for a given temperature gradient, and track the evolution of the temperature gradient.

The EPED1 model, which has successfully predicted the pedestal height and width in several machines, invokes KBM physics as the limiting mechanism for the pressure pedestal gradient. Using the EPED1 model, we show good agreement of the predicted critical gradient with the onset and saturation of the QCF. The observed modes appear to onset once a gradient threshold is reached similar to where KBMs are hypothesized to occur in the EPED1 model. Note that the KBM is predicted to onset with pressure gradient. Here, we observed the QCF to onset with the temperature gradient and subsequently the QCF amplitude tracks and saturates with the temperature gradient evolution.

Several open questions remain. The most obvious one pertains to the exact nature of these fluctuations. The rather narrow radial (~ 1 cm) layer in the high current case cannot exclude magnetic islands at the pedestal top. This mode layer in low current is slightly larger (~ 2 cm) and could still be associated with magnetic islands. Possible mode candidates can be reduced by examining the driving factors. While the temperature gradient appears to correlate with the amplitude evolution of the quasi-coherent fluctuations, it is worth pointing out that the mode onsets when the temperature pedestal gradient reaches a threshold. Such temperature gradient dependence points to either KBM or

micro tearing modes (see Table I of Ref. 40 for characteristics of potential instabilities).

Turning back to ELM and pedestal physics, it is worth noting that quasi-coherent like modes have been previously observed between ELMs on JET.²⁸ Similarly, Alcator, C-Mod observed such QCF between ELMs.²⁶ On DIII-D, BES data show that shortly after an L-H transition, coherent modes turn on.⁹ At the time of turn on, the rise of ∇P_e dramatically slows. The experimental ∇P_e was shown to track the KBM ∇P_e very shortly after the transition. In JET, C-Mod, and DIII-D, the quasi-coherent fluctuations correlate with the pedestal temperature (strictly speaking with its gradient in DIII-D) increase and the density gradient has no apparent effect on the fluctuations' amplitude evolution. C-Mod shows that these low-k fluctuations are localized in the upper part of the steep gradient region (note the pedestal is narrow so a definite localization in the steep gradient region is not certain). On DIII-D, the QCF is also low-k and is observed to be localized at the pedestal region, which within measurement uncertainties could be the pedestal top or the steep gradient region. Initial linear microinstability analysis in the pedestal region using GS2 indicates that the top 1/2 of the steep gradient region is near the KBM threshold with propagation in the electron direction in agreement with QCF propagation as determined using BES. This raises the following questions: Are QCFs a manifestation of KBM or microtearing? It is worth noting that microtearing modes are also sensitive to β_e (see Table I of Ref. 40 for characteristics of potential modes). Thus far, based on the GS2 modeling and observations which clearly show a β_e threshold and a parity consistent with KBM, the results suggest that QCFs are consistent with KBM, but we cannot rule out micro tearing modes as being subdominant. However, addressing this question more systematically will require global nonlinear gyrokinetic calculations in the pedestal region (which have been challenging to perform) and perhaps comparison of the fluctuation spectra with these measurements. Why do QCFs precede ELMs in this case? What make QCFs different from other quasi coherent fluctuations? Indeed, the quasi-coherent nature of these fluctuations is reminiscent of EHO in the QH, QCM in EDA, and WCM on I-mode, with the main exception that all are associated with ELM-free regimes. One of these modes (QCM) has been shown to be localized in the bottom of the pedestal steep gradient using the mirror Langmuir probes on C-Mod.²¹ The EHO is thought to be a saturated kink-peeling mode of low-n,⁴¹ localized in the edge pedestal region. Quasi-coherent fluctuations are observed in the region of the pedestal in the ELMy discharges discussed here and in a number of ELM-free regimes. Future work will investigate the nature of these fluctuations using nonlinear global gyrokinetic calculations (computer intensive) in the pedestal region.

ACKNOWLEDGMENTS

This material was based upon work supported in part by the U.S. Department of Energy, Office of Science, Office of Fusion Energy Sciences, using the DIII-D National Fusion Facility, a DOE Office of Science user facility, under

Awards DE-FC02-04ER54698, DE-AC02-09CH11466, and DE-AC05-00OR22725. DIII-D data shown in this paper can be obtained in digital format by following the links at https://fusion.gat.com/global/D3D_DMP. We thank M.W. Shafer for providing the finite beam lifetime calculations. One of us (A.D.) acknowledges discussions with J. D. Callen.

¹F. Wagner, G. Fussmann, T. Grave, M. Keilhacker, M. Kornherr, K. Lackner, K. McCormick, E. R. Müller, A. Stähler, G. Becker, K. Bernhardt, U. Ditte, Eberhagen, O. Gehre, J. Gernhardt, G. V. Gierke, E. Glock, O. Gruber, G. Haas, M. Hesse, G. Janeschitz, F. Karger, S. Kissel, O. Klüber, G. Lisitano, H. M. Mayer, D. Meisel, V. Mertens, H. Murmann, W. Poschenrieder, H. Rapp, H. Röhr, F. Rytter, F. Schneider, G. Siller, P. Smeulders, F. Söldner, E. Speth, K. H. Steuer, Z. Szymanski, and O. Vollmer, *Phys. Rev. Lett.* **53**, 1453 (1984).

²K. H. Burrell, *Phys. Plasmas* **4**, 1499 (1997).

³J. E. Kinsey, G. M. Staebler, J. Candy, R. E. Waltz, and R. V. Budny, *Nucl. Fusion* **51**, 083001 (2011).

⁴A. W. Leonard, *Phys. Plasmas* **21**, 090501 (2014).

⁵P. B. Snyder, R. J. Groebner, J. W. Hughes, T. H. Osborne, M. Beurskens, A. W. Leonard, H. R. Wilson, and X. Xu, *Nucl. Fusion* **51**, 103016 (2011).

⁶P. B. Snyder, R. J. Groebner, A. W. Leonard, T. H. Osborne, and H. R. Wilson, *Phys. Plasmas* **16**, 056118 (2009).

⁷M. Beurskens, L. Frassinetti, C. Challis, C. Giroud, S. Saarelma, B. Alper, C. Angioni, P. Bilkova, C. Bourdelle, S. Brezinsek, P. Buratti, G. Calabro, T. Eich, J. Flanagan, E. Giovannozzi, M. Groth, J. Hobirk, E. Jorin, M. Leyland, P. Lomas, E. de la Luna, M. Kempnaars, G. Maddison, C. Maggi, P. Mantica, M. Maslov, G. Matthews, M.-L. Mayoral, R. Neu, I. Nunes, T. H. Osborne, F. Rimini, R. Scannell, E. Solano, P. B. Snyder, I. Voitsekhovitch, P. de Vries, and J.-E. Contributors, *Nucl. Fusion* **54**, 043001 (2014).

⁸M. Leyland, M. Beurskens, L. Frassinetti, C. Giroud, S. Saarelma, P. B. Snyder, J. Flanagan, S. Jachmich, M. Kempnaars, P. Lomas, G. Maddison, R. Neu, I. Nunes, and K. Gibson, *Nucl. Fusion* **55**, 013019 (2015).

⁹R. J. Groebner, C. Chang, J. W. Hughes, R. Maingi, P. B. Snyder, X. Xu, J. A. Boedo, D. Boyle, J. Callen, J. M. Canik, I. Cziegler, E. Davis, A. Diallo, P. Diamond, J. D. Elder, D. Eldon, D. Ernst, D. Fulton, M. Landreman, A. W. Leonard, J. Lore, T. H. Osborne, A. Pankin, S. Parker, T. L. Rhodes, S. P. Smith, A. Sontag, W. M. Stacey, J. Walk, W. Wan, E.-J. Wang, J. G. Watkins, A. E. White, D. G. Whyte, Z. Yan, E. A. Belli, B. D. Bray, J. Candy, R. Churchill, T. Deterly, E. J. Doyle, M. E. Fenstermacher, N. M. Ferraro, A. Hubbard, I. Joseph, J. E. Kinsey, B. LaBombard, C. J. Lasnier, Z. Lin, B. Lipschultz, C. Liu, Y. Ma, G. R. McKee, D. Ponce, J. C. Rost, L. Schmitz, G. M. Staebler, L. Sugiyama, J. Terry, M. Umansky, R. E. Waltz, S. Wolfe, L. Zeng, and S. Zweben, *Nucl. Fusion* **53**, 093024 (2013).

¹⁰J. R. Walk, P. B. Snyder, J. W. Hughes, J. L. Terry, A. E. Hubbard, and P. E. Phillips, *Nucl. Fusion* **52**, 063011 (2012).

¹¹J. Hughes, P. Snyder, J. Walk, E. Davis, A. Diallo, B. LaBombard, S. Baek, R. Churchill, M. Greenwald, R. Groebner, A. Hubbard, B. Lipschultz, E. Marmor, T. Osborne, M. Reinke, J. Rice, C. Theiler, J. Terry, A. White, D. Whyte, S. Wolfe, and X. Xu, *Nucl. Fusion* **53**, 043016 (2013).

¹²P. B. Snyder, T. H. Osborne, K. H. Burrell, R. J. Groebner, A. W. Leonard, R. Nazikian, D. M. Orlov, O. Schmitz, M. R. Wade, and H. R. Wilson, *Phys. Plasmas* **19**, 056115 (2012).

¹³P. B. Snyder, N. Aiba, M. Beurskens, R. J. Groebner, L. D. Horton, A. E. Hubbard, J. W. Hughes, G. T. A. Huysmans, Y. Kamada, A. Kirk, C. Konz, A. W. Leonard, J. Lönnroth, C. F. Maggi, R. Maingi, T. H. Osborne, N. Oyama, A. Pankin, S. Saarelma, G. Saibene, J. L. Terry, H. Urano, and H. R. Wilson, *Nucl. Fusion* **49**, 085035 (2009).

¹⁴R. J. Groebner, T. H. Osborne, A. W. Leonard, and M. E. Fenstermacher, *Nucl. Fusion* **49**, 045013 (2009).

¹⁵A. Diallo, R. Maingi, S. Kubota, A. Sontag, T. Osborne, M. Podestá, R. E. Bell, B. P. LeBlanc, J. Menard, and S. Sabbagh, *Nucl. Fusion* **51**, 103031 (2011).

¹⁶A. Burckhart, E. Wolfrum, R. Fischer, K. Lackner, H. Zohm, and the ASDEX Upgrade Team, *Plasma Phys. Controlled Fusion* **52**, 105010 (2010).

¹⁷A. Kirk, T. O'Gorman, S. Saarelma, R. Scannell, H. R. Wilson, and the MAST Team, *Plasma Phys. Controlled Fusion* **51**, 065016 (2009).

- ¹⁸K. H. Burrell, T. H. Osborne, P. B. Snyder, W. P. West, M. E. Fenstermacher, R. J. Groebner, P. Gohil, A. W. Leonard, and W. M. Solomon, *Phys. Rev. Lett.* **102**, 155003 (2009).
- ¹⁹A. E. Hubbard, R. L. Boivin, R. S. Granetz, M. Greenwald, J. W. Hughes, I. H. Hutchinson, J. Irby, B. LaBombard, Y. Lin, E. S. Marmor, A. Mazurenko, D. Mossessian, E. Nelson-Melby, M. Porkolab, J. A. Snipes, J. Terry, S. Wolfe, S. Wukitch, B. A. Carreras, V. Klein, and T. Sunm Pedersen, *Phys. Plasmas* **8**, 2033 (2001).
- ²⁰D. G. Whyte, A. E. Hubbard, J. W. Hughes, B. Lipschultz, J. E. Rice, E. S. Marmor, M. Greenwald, I. Cziegler, A. Dominguez, T. Golfinopoulos, N. Howard, L. Lin, R. M. McDermott, M. Porkolab, M. L. Reinke, J. Terry, N. Tsujii, S. Wolfe, S. Wukitch, Y. Lin, and the Alcator C-Mod Team, *Nucl. Fusion* **50**, 105005 (2010).
- ²¹B. LaBombard, T. Golfinopoulos, J. L. Terry, D. Brunner, E. Davis, M. Greenwald, J. W. Hughes, and Alcator C-Mod Team, *Phys. Plasmas* **21**, 056108 (2014).
- ²²D. Eldon, B. D. Bray, T. M. Deterly, C. Liu, M. Watkins, R. J. Groebner, A. W. Leonard, T. H. Osborne, P. B. Snyder, R. L. Boivin, and G. R. Tynan, *Rev. Sci. Instrum.* **83**, 10E343 (2012).
- ²³T. H. Osborne, P. B. Snyder, K. H. Burrell, T. E. Evans, M. E. Fenstermacher, A. W. Leonard, R. A. Mpyer, M. J. Schaffer, and W. P. West, *J. Phys.: Conf. Ser.* **123**, 012014 (2008).
- ²⁴M. R. Wade, K. H. Burrell, J. T. Hogan, A. W. Leonard, T. H. Osborne, P. B. Snyder, and D. Coster, *Phys. Plasmas* **12**, 056120 (2005).
- ²⁵W. M. Solomon, K. H. Burrell, A. M. Garofalo, R. J. Groebner, C. J. Lasnier, M. A. Makowski, T. H. Osborne, H. Reimerdes, J. S. deGrassie, E. J. Doyle, T. E. Evans, M. E. Fenstermacher, G. L. Jackson, and M. J. Schaffer, *Nucl. Fusion* **52**, 033007 (2012).
- ²⁶A. Diallo, J. W. Hughes, M. Greenwald, B. LaBombard, E. Davis, S-G. Baek, C. Theiler, P. Snyder, J. Canik, J. Walk, T. Golfinopoulos, J. Terry, M. Churchill, A. Hubbard, M. Porkolab, L. Delgado-Aparicio, M. L. Reinke, A. White, and Alcator C-Mod team, *Phys. Rev. Lett.* **112**, 115001 (2014).
- ²⁷P. Smeulders, G. D. Conway, B. Alper, B. Balet, D. V. Bartlett, D. Barba, N. Deliyanakis, T. C. Hender, and O. J. Kwon, *Plasma Phys. Controlled Fusion* **41**, 1303 (1999).
- ²⁸C. P. Perez, H. R. Koslowski, T. C. Hender, P. Smeulders, A. Loarte, P. J. Lomas, G. Saibene, R. Sartori, M. Becoulet, T. Eich, R. J. Hastie, G. T. A. Huysmans, S. Jachmich, A. Rogister, F. C. Schüller, and J. E. Contributors, *Plasma Phys. Controlled Fusion* **46**, 61 (2004).
- ²⁹Z. Yan, G. R. McKee, R. J. Groebner, P. B. Snyder, T. H. Osborne, and K. H. Burrell, *Phys. Rev. Lett.* **107**, 055004 (2011).
- ³⁰Z. Yan, G. R. McKee, R. J. Groebner, P. B. Snyder, T. H. Osborne, M. N. Beurskens, and K. H. Burrell, *Phys. Plasmas* **18**, 056117 (2011).
- ³¹M. Hirsch, E. Holzauer, J. Baldzuhn, B. Kurzan, and B. Scott, *Plasma Phys. Controlled Fusion* **43**, 1641 (2001).
- ³²E. Holzauer, M. Hirsch, T. Grossmann, B. Brañas, and F. Serra, *Plasma Phys. Controlled Fusion* **40**, 1869 (1998).
- ³³M. Kotschenreuther, G. Rewoldt, and W. M. Tang, *Comput. Phys. Commun.* **88**, 128 (1995).
- ³⁴J. M. Canik, W. Guttenfelder, R. Maingi, T. H. Osborne, S. Kubota, Y. Ren, R. E. Bell, H. W. Kugel, B. P. LeBlanc, and V. A. Souhkanovskii, *Nucl. Fusion* **53**, 113016 (2013).
- ³⁵D. Dickinson, C. M. Roach, S. Saarelma, R. Scannell, A. Kirk, and H. R. Wilson, *Phys. Rev. Lett.* **108**, 135002 (2012).
- ³⁶W. Guttenfelder, J. L. Peterson, J. Candy, S. M. Kaye, Y. Ren, R. E. Bell, G. W. Hammett, B. P. LeBlanc, D. R. Mikkelsen, W. M. Nevins, and H. Yuh, *Nucl. Fusion* **53**, 093022 (2013).
- ³⁷W. Wan, S. E. Parker, Y. Chen, Z. Yan, R. J. Groebner, and P. B. Snyder, *Phys. Rev. Lett.* **109**, 185004 (2012).
- ³⁸E. Wang, X. Xu, J. Candy, R. J. Groebner, P. B. Snyder, Y. Chen, S. Parker, W. Wan, G. Lu, and J. Dong, *Nucl. Fusion* **52**, 103015 (2012).
- ³⁹A. Pigarov, S. Krasheninnikov, T. Rognlien, C. J. Lasnier, and E. A. Unterberg, "Dynamic plasma-wall modeling of ELMy H-mode with UEDGE-MB-W," *J. Nucl. Mater.* (published online).
- ⁴⁰P. Manz, J. E. Boom, E. Wolfrum, G. Birkenmeier, I. G. J. Classen, N. C. Luhmann, Jr., U. Stroth, and the ASDEX Upgrade Team, *Plasma Phys. Controlled Fusion* **56**, 035010 (2014).
- ⁴¹K. H. Burrell, T. H. Osborne, P. B. Snyder, W. P. West, M. E. Fenstermacher, R. J. Groebner, P. Gohil, A. W. Leonard, and W. M. Solomon, *Nucl. Fusion* **49**, 085024 (2009).